Manufacturing of nano-reinforced aluminium composites by a combination of stir mixing, ultrasonic processing and high-pressure die casting

Guangyu Liu*, Mahfuz Karim, Dmitry Eskin, Brian McKay

Brunel Centre for Advanced Solidification Technology, Brunel University London, Uxbridge, Middlesex, UB8 3PH, United Kingdom

**Corresponding author, E-mail address: guangyu.liu2@brunel.ac.uk.*

Abstract

Due to their high specific strength, aluminium-based metal matrix nanocomposites reinforced with ceramics are an attractive proposition for applications in the transport sector. High Pressure Die Casting (HPDC) is a cost-effective manufacturing route for the mass production of aluminium castings exhibiting complex near-net-shape geometries. Through the application of high pressure and high cooling rates, improved distribution of the reinforcing particles compared to other casting methods can be attained. This is a result of the increased filling capacity of the composite melt and the resultant finer grain structure. In this study, an AlSi9Cu3 (LM24) commercial alloy was reinforced with SiC nanoparticles. The reinforcement was introduced using novel Al-nanoSiC alloys and processed using stir mixing, ultrasonic processing and HPDC technologies to achieve enhanced mechanical properties. The results showed the good distribution of the loose SiC agglomerates, demonstrating a nearly 40% reduction in the Al grain size, from ~23.7µm to ~14.8 µm, and indicating a ~15MPa and ~18MPa increment in the yield strength (YS) and the ultimate tensile strength (UTS), due to a combined effect of the grain refinement, CTE strengthening and Orowan strengthening.

Keywords: Aluminum MMnCs, Stir mixing, Ultrasonication, HPDC

1 Introduction

With a combination of the ductility and toughness of the aluminium matrix and the superior strength and stiffness of the ceramic reinforcements, the aluminium-based metal matrix composites (AMMCs) have been widely developed in automotive and aerospace industries [1,2]. The particulate reinforced AMMCs are of great interest because they display isotropic mechanical properties and are easier to manufacture and often cheaper in comparison with the continuous fibre reinforced AMMCs [3]. These reinforcements are typically ceramic particles including oxides, carbides, and nitrides, such as Al_2O_3 [4], TiO_2 [5], SiO_2 [6], B_4C [7], TiC [8], SiC [9], Si_3N_4 [10], and AlN [11] etc. Among them, the SiC and Al_2O_3 particles are mostly applied compared to other reinforcing particulates. Preferably, the SiC particle is known to exhibit higher elastic modulus and specific strength, superior wear resistance and stiffness, and greater thermal conductivity over Al_2O_3 [12], making the Al/SiC_p composites more popular for the parts that require extremely high wear resistance and thermal conductivity, such as pistons, brake rotors, and the propeller shaft [13].

The reinforcing particulates often strengthen the aluminium composites in two approaches. One is the classical load transfer [14], through carrying the loading along with aluminium matrix, the contribution of which can be principally significant in the presence of high-volume reinforcements with coarse sizes. The other is the micromechanics-based mechanism being in association with dislocation activities, i.e., Orowan strengthening and coefficient of thermal expansion (CTE) mismatch strengthening. This is particularly dominant in the composites reinforced by fine particles (<1 μm) [15]. In specific, the Orowan strengthening is based on the resistance of small hard particles against the motion of dislocations, the dislocation movement proceeds with passing by these obstacles by bowing, reconnecting, and forming a dislocation loop around the particles, leading to high work-hardening rates with improved strength [16,17]. The strengthening effectiveness can be considerably boosted when the reinforcing particles are uniformly dispersed and the interspacing of the particles are sufficiently small [18]. On the other hand, when an AMMC is quenched from the processing temperature to room temperature, volumetric strain mismatch between the monolithic matrix and reinforcing particles may occur due to differences in CTE, which will subsequently produce geometrically necessary dislocations (GND) around reinforcing particles to accommodate the CTE difference [19,20]. Similarly, during the cooling of the AMMC in the solidification process, a great number of dislocations can be generated due to thermal mismatch between the matrix and the reinforcing particles [21], strengthening the composites. In addition, the grain refinement effect caused by the addition of nanoparticles that might potentially introduce more nucleation sites and/or provide agglomerates as the obstacles to grain growth during solidification plays a critical role in the increased strength by the Hall–Petch strengthening effect [22,23].

It has been well established that the effectiveness of strengthening is significantly dependant on the amount, size, and distribution of the reinforcing particles [24]. Microscale reinforcing particles often improve the strength but simultaneously decrease the ductility and toughness, resulting in a trade-off between strength and ductility, while the ductility and toughness of AMMCs can be significantly improved with a concurrent increase in strength by reducing the particle size to nanoscale. On the other hand, when the particle size is reduced to nanoscale, particle agglomeration/clustering, high porosity content, and weak particle/matrix interface bond usually occur in the AMMCs casting process, arising from the stir preparation, mould filling, and solidification stages [25,26,27]. These in-perfections are detrimental to the mechanical properties [28]. For example, the clusters can act as cracks

or de-cohesion nucleation sites, or both, at stress lower than matrix yield strength, causing the AMMCs to fail at unpredictable low-stress levels [29,30]. Most importantly, due to poor wetting of the nanoparticles by the molten metal, and the formation of clusters of nanoparticles in the melt from the Van der Waals attraction force, it is sometimes infeasible to uniformly disperse the nanoparticles in the molten matrix during the traditional casting process.

Stir casting combined with ultrasonic processing has been considered a promising method for decent dispersion of nanoparticles in the molten matrix [31]. During ultrasonic treatment, acoustic waves generate tensile stress in the molten metal, leading to the formation of tiny cavities. During the expansion cycles, the cavities grow whereas during the compression cycles they collapse and produce transient (in the order of microseconds) micro "hot spots", where extremely high temperatures (5000 ºC) and pressures (~1000 atm) are generated [32]. This process is so-called "acoustic cavitation" that can generate high-density shock waves to break the agglomerates/clusters and disperse them under acoustic streaming [33]. Besides, the local transient high temperature and pressure could significantly improve the wettability of particles by removing or desorbing the gases from the surface of the particles. It increases the surface energy of nanoparticles in the vapour phase. At a very high temperature (5000 °C), the surface tension of liquid with vapour is significantly decreased which further enhances the wettability of the nanoparticles [15,34].

High pressure die casting has been deemed a cost-effective and productive manufacturing technique for mass production of aluminium castings with a complex near-net-shape [35]. It is especially suitable for the components requiring high dimensional accuracy and no post-machining process. These characteristics make it even more suitable for producing AMMCs achieving a near-net-shape forming for decreasing post-machining, given the poor machinability of the composites [36]. Also, the high pressure applied in HPDC improves the filling capacity of the molten composites, in which the fluidity is generally decreased due to the addition of particles. Meanwhile, the fine grain structure is beneficial to the distribution of the reinforcing nanoparticles during solidification. Li et al [37] reported the carbon nanotubes (CNTs) reinforcements could be dispersed by high turbulent flow in the cavity through HPDC, by locating the pre-dispersed CNTs on the entrance of the die cavity, to successfully manufacture the Al/CNTs composites. Hu et al [38] have suggested the improved particle distribution, decrease of porosity, and matrix/particle interface with good bonding, the properties of the HPDC Al/SiC_p composites (100 μm) show a significant improvement compared to the sample by gravity casting.

This study aimed to prepare LM24 (AlSi9Cu3)-based SiC_{np} reinforced nanocomposites with good dispersion of the SiC nanoparticles and improved mechanical properties, by combining the advantages of stir mixing, ultrasonic processing and HPDC technology. Notably, instead of applying loose nanoparticles, the Al-Cu-SiC_{np} master alloys were employed as the nanoparticle sources, in attempts to improve the introduction and dispersion of the SiC particles. The distribution and effects of SiC nanoparticles on the resultant microstructure and mechanical properties were thoroughly investigated.

2 Experimental

2.1 Sample preparations

Al-50Si andAlSi8Cu3 ingots (supplied by Norton Aluminium Ltd., UK) were chosen as the raw materials to produce aluminium matrix melt. The Al-Cu and Al-Cu-SiC_{np} master alloys being in the respective form of granule (5-10 mm) and small shots (100-2000 µm), as shown in Figure 1a and 1b, was added to the individual melt to prepare the baseline alloy and the SiC_{np} reinforced composites, respectively. The chemical composition of the baseline alloy and the composite was shown in Table 1. The SiC particles were in nanoscales (< 100 nm).

Table 1 Composition of the LM24 (base) alloy and the LM24/SiC_{np} composite measured by foundry master, wt%.

Materials	Al	Si	Cu	Fe	Mn	Mg	Ti	Zn	Ni	Others
Base	Bal	8.89	3.92	1.13	0.31	0.11	0.09	1.59	0.04	<0.001
LM24/SiC_{np}	Bal	9.12	4.01	1.29	0.29	0.10	0.09	1.50	0.04	<0.001

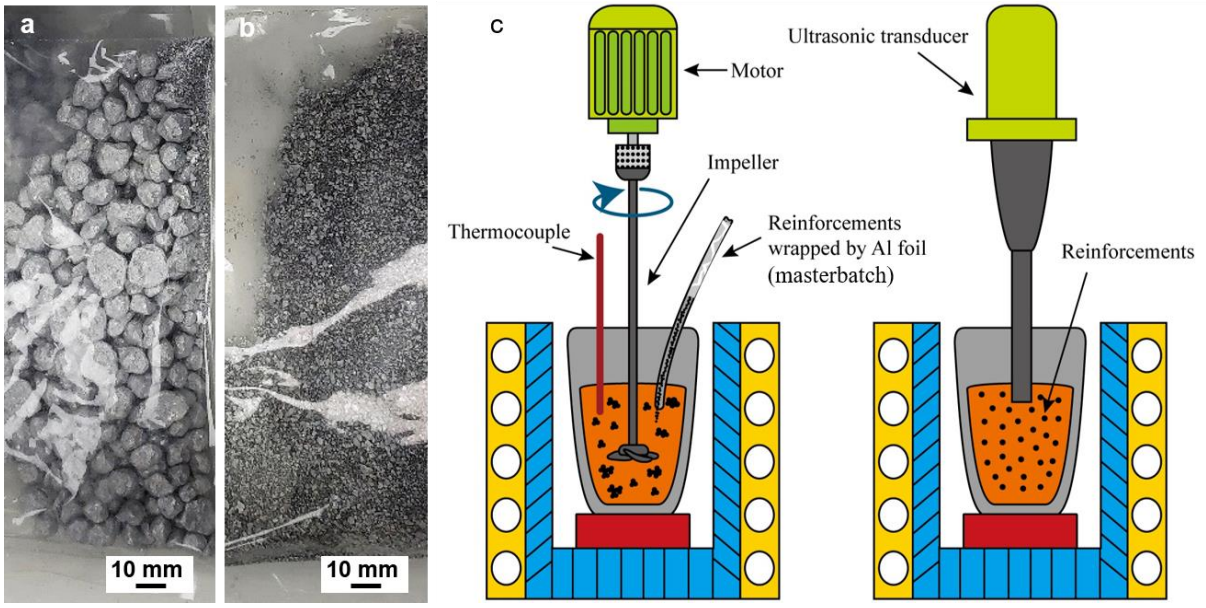

Figure 1 The photos and schematics showing (a) the Al-Cu masterbatch in the form of granule: 5-10 mm, (b) the Al-Cu-SiC_{np} master alloy in the form of small shots: 100-2000 µm, and (c) the stir mixing process assisted by the ultrasonic treatment.

Figure 1c shows the schematic experimental setup for making the AMMnCs by ultrasound-assisted solidification technique, which consists of an electric resistance furnace, impeller-rotor unit, and ultrasonic unit. A total amount of ~3kg of the LM24 ingots and Al-50Si alloys was put in the crucible and melted in an electrical resistance furnace (Carbolite) at 750 °C. After the melt was homogenised for approximately 2 hours, the preheated (at 300 °C) Al-Cu-SiC_{np} master powders wrapped in Al foil were fed into the melt at the side of the vortex created by a four-bladed titanium impeller rotating in the clockwise direction, to achieve a pre-mixing and preliminary introduction of nanoparticles in the melt. The impeller was coated with boron nitride to prevent the reaction with

molten aluminium. In the stir mixing process, nominal ~1wt% SiC nanoparticles were successfully introduced into the melt, producing the composite melt, with the melt temperature decreased from 750 ºC to 650 ºC in the time range of 6 minutes. Then, the pre-mixed composite melt was reheated up to 750 ºC before it was ultrasonically processed. A 20 kHz ultrasonic wave transmitted by a 19 mm diameter niobium probe generated with a 1.8 kW capacity ultrasonic generator unit was applied to the melt for 10 min to achieve a further dispersion of nanoparticles. After ultrasonic processing, the melt temperature dropped to 700 ºC. After holding for 1 minute, the composite melt was manually poured into the shot sleeve to produce tensile samples of 6.35 mm in diameter by a Frech 4500 kN locking force cold chamber HPDC machine. The pouring temperature of the melt, die temperature, and shot sleeve temperature was 700 ± 5 °C, 200 ± 5 °C and 180 ± 5 °C respectively. The baseline alloy was produced in the same process except that no SiC master alloys were added.

2.2 Mechanical test

Vickers hardness tests were conducted on the cross-section of the gauge section of the casting bars, by using a Wilson 432SVA digital auto turret macro Vickers Hardness Tester. Each specimen was applied to a 10 N load and a dwell time of 10 s. Tensile testing was carried out on an Instron 5500 Universal electromechanical testing system at ambient temperature. A gauge length of 50 mm and a gauge diameter of 6.35 mm were applied. The ramping rate was 1 mm/min, and a 50 mm extensometer was used to record tensile data. Each data reported with standard deviation was based on the mechanical properties attained from 12 to 15 samples.

2.3 Microstructure characterisation

The metallurgical microstructural examination was conducted on the cross-section of Al-Cu, Al-Cu-SiC_{np} master alloys, and the casting bars at the gauge positions. The surface to be examined was ground using SiC abrasive papers and then polished using silica suspension (OPS, 0.05 µm water-based SiO_2 suspension). Quantitative analysis of the microstructure was performed using AxioVision Rel. 4.8 software. Detailed information on intermetallic phases, reinforcing nanoparticles and grain structures was obtained using the Zeiss Supra 35 field-emission scanning electron microscope (FESEM), equipped with energy-dispersive X-ray spectroscopy (EDS). Nano-scaled precipitates and nanoparticles were examined using high-resolution transmission electron microscopy, JEOL 2100F (JEOL Ltd.). The TEM samples were cut from LM24 and LM24/SiC_{np} specimens and were ground to less than 100 µm thicknesses. 3 mm diameter samples were punched, and the further reduction of thickness was obtained by Gatan precision ion polishing system (PIPS) adjusted at 5.0 kV and an incident angle of 3-5°.

3 Results

3.1 Microstructure of the Al-Cu and Al-Cu-SiC_{np} master alloys

Figure 2 presents the SEM micrographs showing the intermetallic phase and SiC particles in the microstructure of Al-Cu and Al-Cu-SiC_{np} master alloys. The microstructure of Al-Cu mainly comprised the Al phase (dark), Al_2Cu phase (grey), and Cu phase (white), as indicated in Figure 2a. In the microstructure of Al-Cu-SiC_{np}, fine Al_2Cu phase with the size of 3-8µm were readily observed, while the white Cu phase was absent (Figure 2b). It was observed from Figure 2c that extensive fine particles (white) were homogeneously distributed in the matrix. With closer inspection of the microstructure (Figure 2d), these particles displayed irregular shapes with the size

being less than 100 nm, which were identified as the SiC nanoparticles, as indicated by the EDS results (inset). This indicated that the SiC nanoparticles were uniformly distributed in the Al-Cu-SiC_{np} master alloy, which was expected to improve the distribution of the particles in the melt during the stir mixing process.

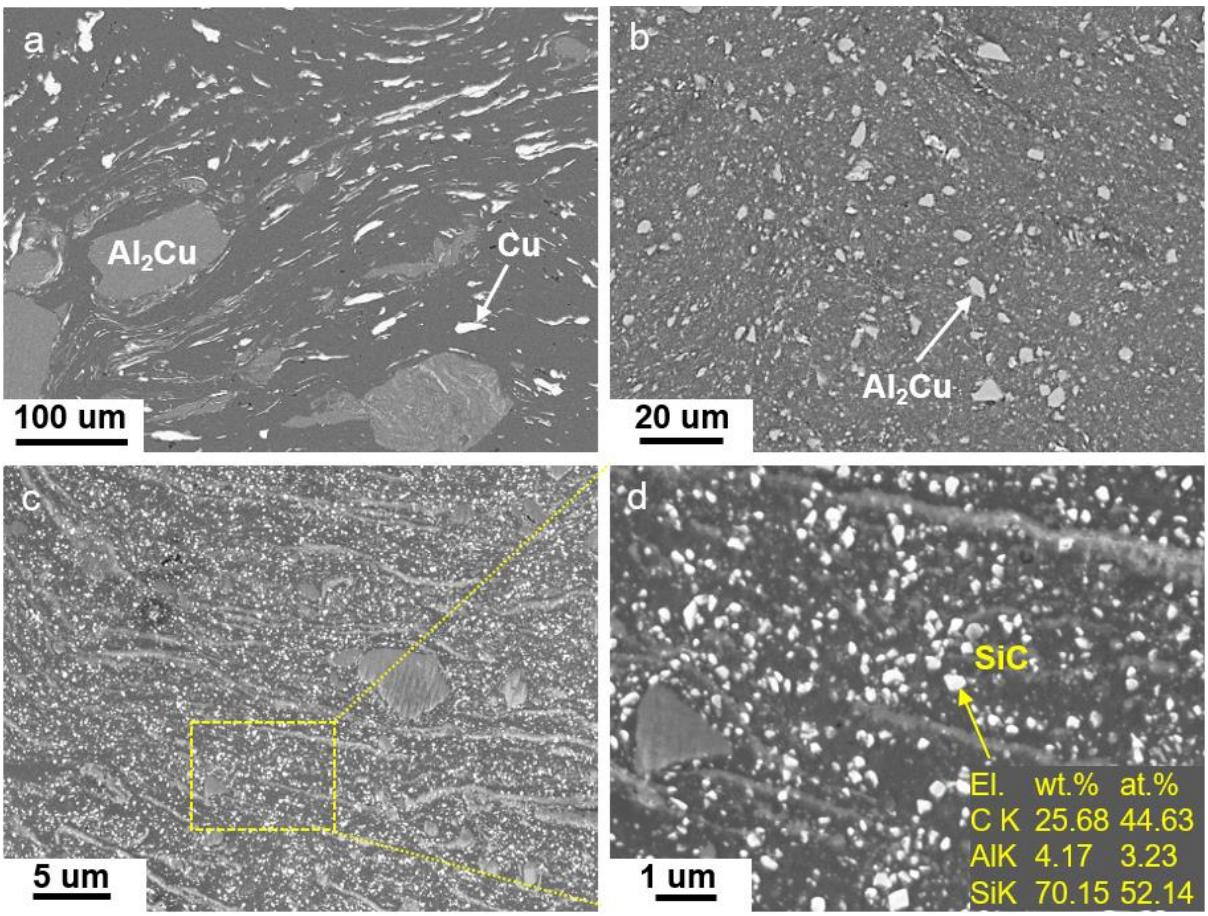

Figure 2 SEM micrographs showing the intermetallic phase and the SiC nanoparticles in the microstructure of (a) Al-Cu and (b, c, d) Al-Cu-SiC_{np} master alloy; (a, b) BSE mode and (c, d) In-lens mode.

3.2 Microstructure of the LM24 alloy and LM24/SiC_{np} composite

3.2.1 α-Al grains, eutectic and porosities

Figure 3 compares the microstructural features including the primary α-Al phases, Al-Si eutectic, and porosities in the LM24 alloy and LM24/SiC_{np} composite. It was observed that the primary α-Al phase exhibited two forms, i.e., coarse Al(α_1) grains nucleated in the shot sleeve with low cooling rates and the fine Al(α_2) grains formed in die cavity with high cooling rates. For the LM24 alloy, some coarse Al(α_1) grains were found in the form of dendrites with the size of 50-100 µm, as indicated in Figure 3a and 3b, while the coarse Al(α_1) grains observed in the LM24/SiC_{np} exhibited less dendritic morphology with smaller sizes of 30-50 µm, as indicated in Figure 3c, and 3d. The morphology of the fine Al(α_2) grains in both samples showed equiaxial grains with the size being less than ~10 µm. A lower proportion of the coarse Al(α_1) grains was present in the LM24/SiC_{np} composite in comparison with that in the LM24 alloy, indicating that the addition of SiC nanoparticles benefits refinement of the primary Al(α_1) phase. Pores are commonly obtained in the HPDC process, both samples present relative

amounts of pores but a higher proportion was attained in the LM24/SiC$_{np}$ composite, which was ascribed to the entrapment of the air during the process of stir mixing.

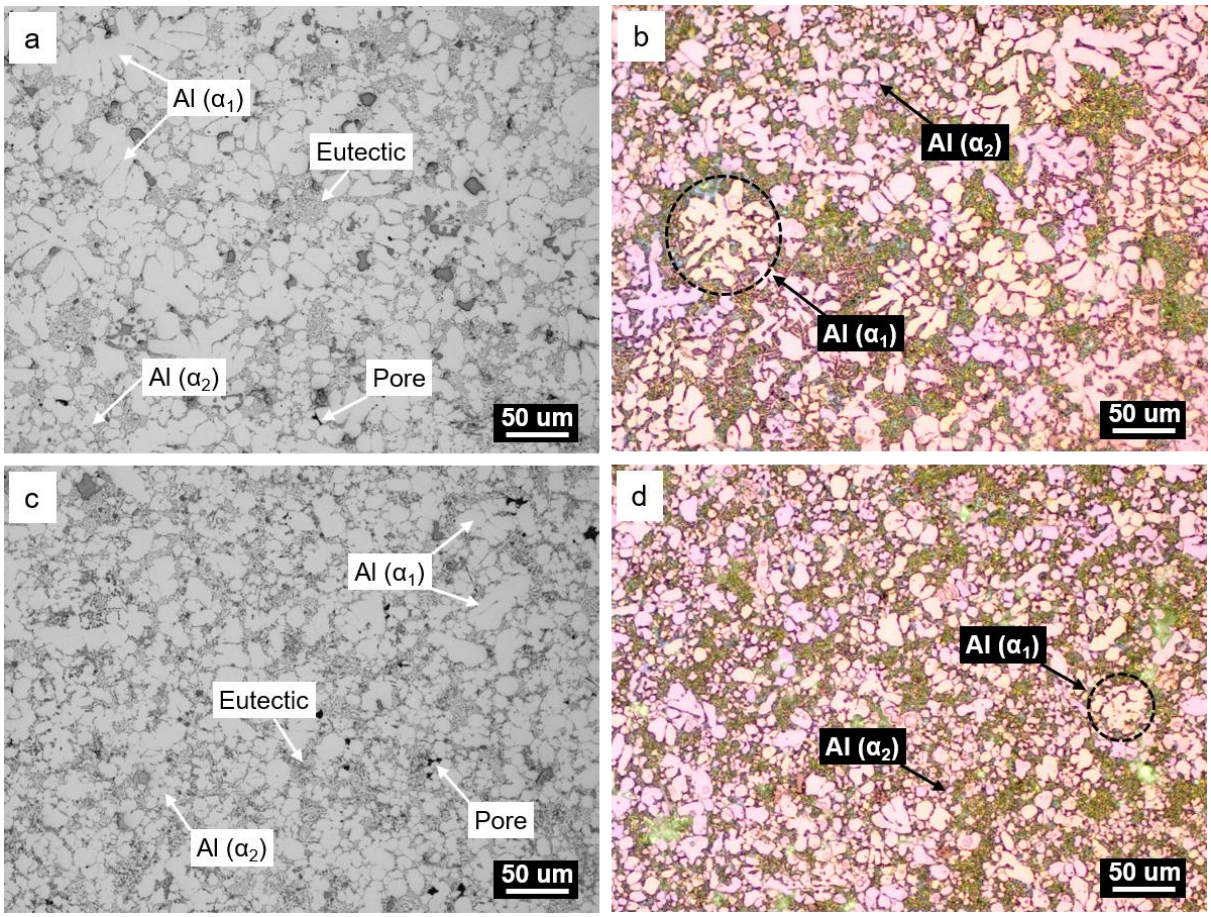

Figure 3 Optical micrographs showing the size and morphology of the primary α-Al phase, eutectics and porosities in the (a, b) LM24 alloy and (c, d) LM24/SiC$_{np}$ composite; (b) and (d) are obtained in the polarized surface.

Figure 4 shows the EBSD grain maps and the grain size distribution in the LM24 alloy and LM24/SiC$_{np}$ composite. The grain tolerance angle is set to be 15^{o} to distinguish the neighbouring grains which are highlighted by different colours, as shown in Figure 4a and 4b. The respective Al grain size in the LM24 alloy and LM24/SiC$_{np}$ composite was measured to be ~23.7 μm and ~14.8 μm (Figure 4c and 4d), indicating a significant grain refinement by the addition of SiC nanoparticles.

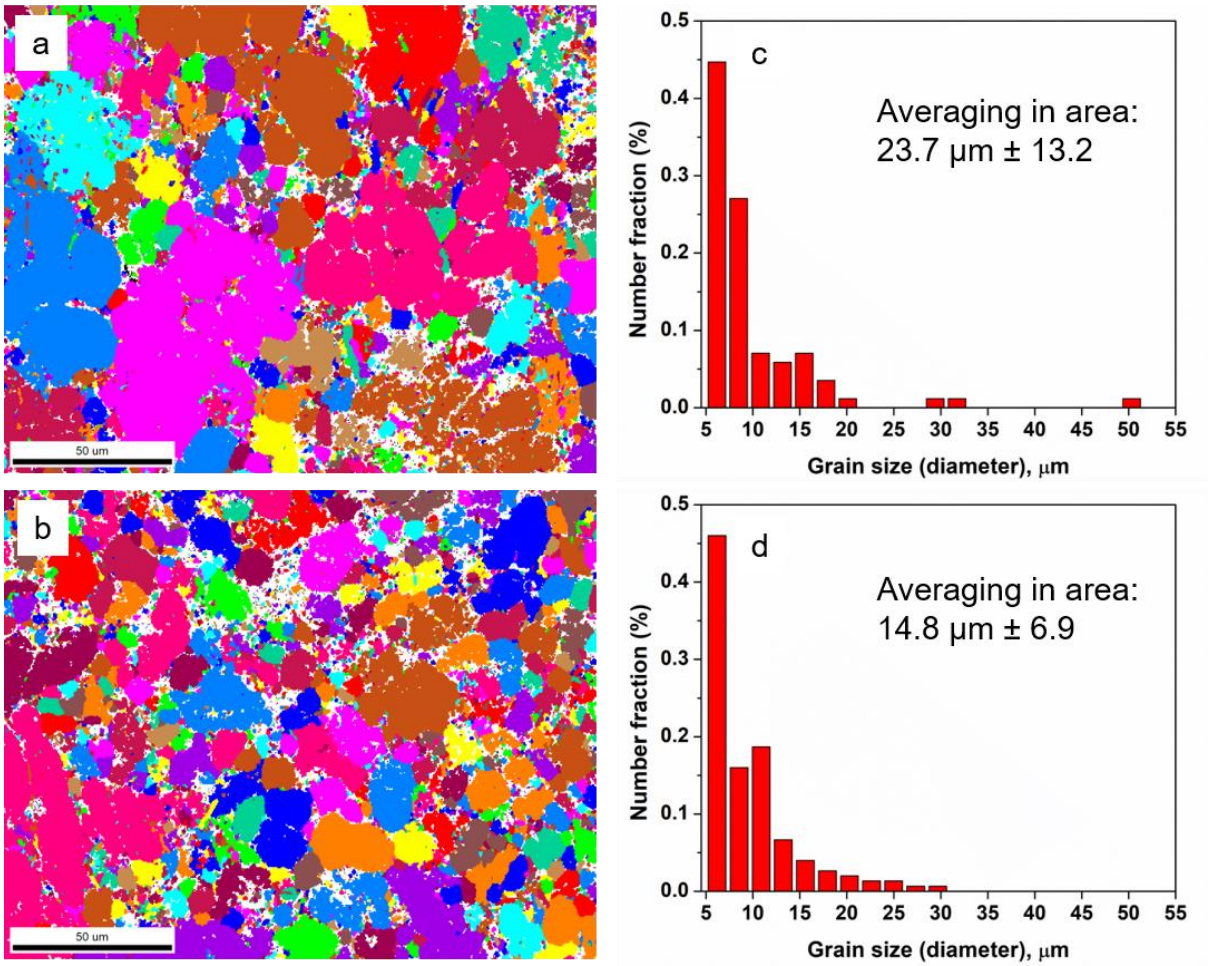

Figure 4 The EBSD grain map and grain size distribution diagram obtained in the microstructure of (a, b) LM24 alloy and (c, d) LM24/SiC_{np} composite. Grain Tolerance Angle: 15.

3.2.2 Secondary phases and SiC nanoparticles

Figure 5 shows the size and morphology of the Fe-bearing and Cu-bearing intermetallic phase and eutectic Si particles in the LM24 alloy. The blocky Al_2Cu phase, the needle-like β-Al_5FeSi phase with the size of ~10 μm, and the coarse polygon-shaped α-Fe_1 ($Al_{15}(Fe, Mn)_3Si_2$) phase with the size of 5-10 μm were readily observed (Figure 5a). In addition to the coarse α-Fe_1 phase, other fine α-Fe_2 particles displaying the equiaxial shape with the size of about 0.5-1 μm were present, as highlighted by the dotted circle in Figure 5a. The corresponding chemical compositions of the individual Fe-bearing and Cu-bearing intermetallic phases highlighted by S1, S2, and S3 were analysed by EDS, as shown in Figure 5c, 5d, and 5e. It is suggested that two types of Fe-bearing intermetallic phase can be formed during different stages of solidification for the LM24 alloys [39]. The coarse Fe-bearing intermetallic phase forms in the shot sleeve, usually displaying polyhedral or block-shaped morphology, while the pro-eutectic Fe-bearing intermetallic phase is often nucleated and solidified in the die cavity, exhibiting polyhedral and/or hexagonal morphology with fine size. From Figure 5, the readily observed coarse α-Fe_1 intermetallic phase exhibiting the polyhedral or blocky morphology should be the primary ones formed in the shot sleeve and the fine α-Fe_2 intermetallic phase should be the secondary ones formed in the die cavity with a higher cooling rate. It is noted that the fine α-Fe_2 phase showed a less ratio of (Fe, Mn) to Si than the primary coarse α-Fe_1 phase, as indicated by the EDS results (Figure 5c and 5d), indicating a lower level of Fe

and Mn element in α-Fe_2 phase. This is consistent with the fact that at the late stage of solidification, fewer Fe and Mn atoms were available for the formation of the pro-eutectic α-Fe_2 phase, due to large consumption by the α-Fe_1 phase. The acicular networked fibrous Si eutectic Si phase can be observed, as indicated by the yellow circle in Figure 5b.

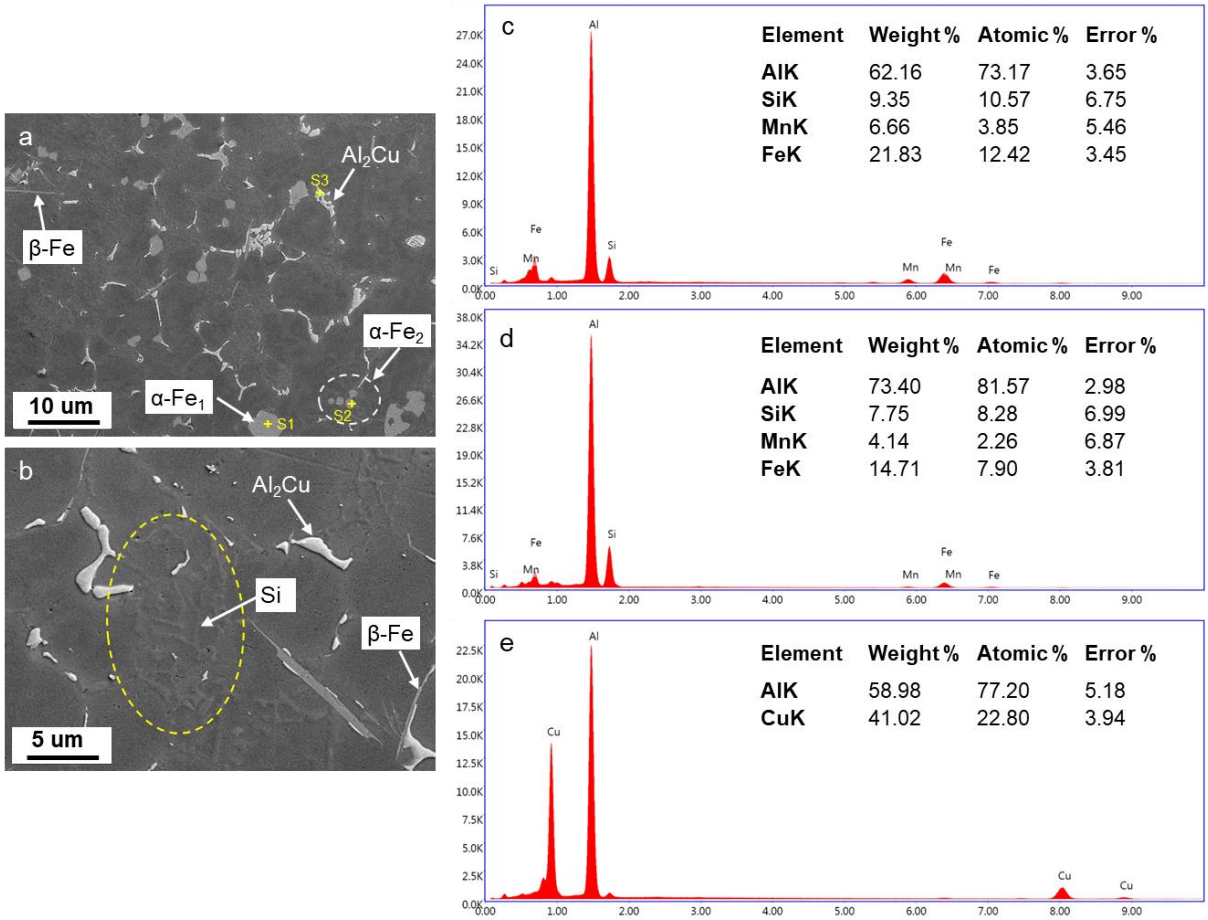

Figure 5 (a, b) SEM micrographs showing Fe-bearing, Cu-bearing intermetallic phase, and eutectic Si phase in the LM24 alloy; (c), (d), (e) the EDS analysis results of the Fe-bearing and Cu-bearing intermetallic phases corresponding to the spectrums S1, S2, and S3.

Figure 6 presents the SEM and TEM micrographs showing the distribution of SiC nanoparticles and secondary phases in the LM24/SiC_{np} composite. Overall, loose SiC clusters/agglomerates were homogeneously distributed in the matrix, as indicated in the region highlighted by the white-dashed circles in Figure 6a. These SiC clusters were dispersed mainly in the interdendritic and Al-Si eutectic regions. It is clear from Figure 6b and 6c that the Al-Si eutectic region was enriched with loose SiC clusters, eutectic Si phase, and fine pro-eutectic α-Fe_2 particles. From the TEM micrograph (Figure 6d), it is found that a small amount of individual SiC nanoparticles can be agglomerated to form clusters in the vicinity of α-Fe_2 particles. The EDS results confirmed these particles were SiC phase (not shown here), displaying similar sizes and morphologies to the SiC particles observed in the master alloys (Figure 2d). Also, the blocky Al_2Cu phase, needle-like β-Al_5FeSi phase, and the fine polygon-shaped α-Fe_2 phase were readily seen as shown by the arrows.

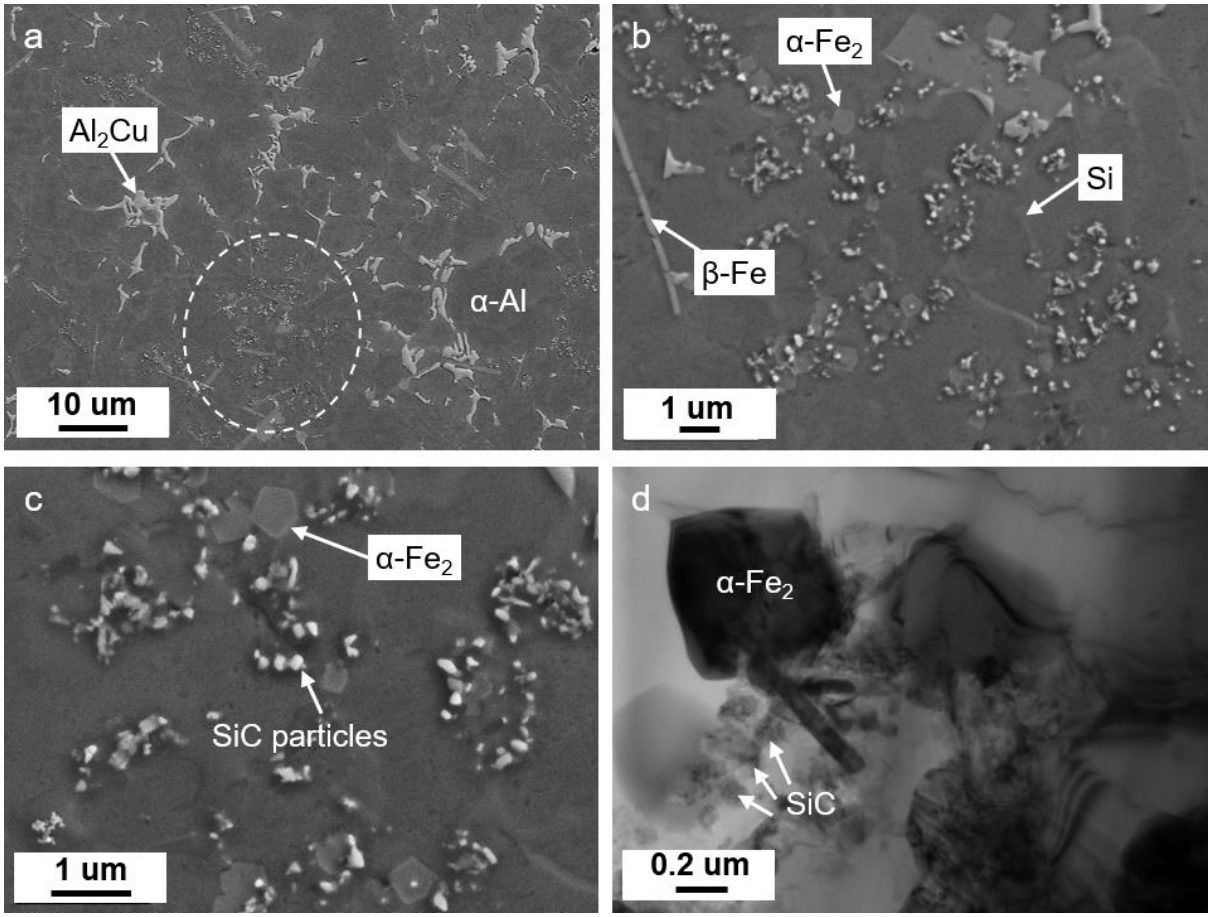

Figure 6 (a, b, c) SEM and (d) TEM micrographs showing the SiC nanoparticles, eutectic Si phase, Fe-rich and Cu-rich intermetallic phases in the LM24/SiC_{np} composites.

3.3 Hardness of the LM24 alloy and LM24/SiC_{np} composite

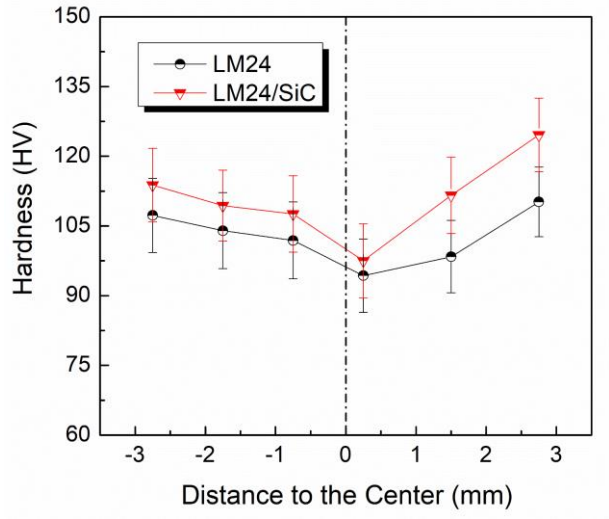

Figure 7 HV hardness variation with the change in distance from the centre to the edge of the cross-section of the LM24 alloy and LM24/SiC_{np} composite.

Figure 7 shows Vickers hardness of the LM24 alloy and LM24/SiC$_{np}$ composite. The indentations were conducted across through the centre of the cross-section of the sample from one edge to another. In both specimens, the hardness exhibited an inhomogeneous distribution from the edge to the centre, showing higher values in the region near the edge. The inhomogeneous distribution of the hardness was originated from the inhomogeneous microstructure across the cross-section. The region being close to the edge experienced a higher solidification rate, leading to a finer microstructure, which resulted in higher hardness. In comparison with the LM24 alloy, the measured hardness was increased consistently in the identical positions in the LM24/SiC$_{np}$ composite, indicating the strengthening effect by the addition of SiC particles. Specifically, for the LM24, the hardness value ranged from HV94.3 to HV110.2, averaging at HV102.6, while this was increased to HV97.5-HV124.6, averaging at HV110.5, increased by 7.7%.

3.4 Tensile properties of the LM24 alloy and LM24/SiC$_{np}$ composite

Figure 8a shows the tensile stress-strain curves for the LM24 and LM24/SiC$_{np}$ samples. The addition of SiC nanoparticles led to an increase in strength and a slight decrease in ductility. This was in agreement with the variation in hardness. The corresponding detailed tensile results were summarised in Figure 8b. The yield strength (YS) of as-cast LM24 was 172.8 MPa, which was increased by ~8% to 186.6 MP with the addition of SiC nanoparticles. At the same time, the ultimate tensile strength (UTS) was increased from 332.5 MPa to 349.6 MPa (by ~5.1%). The respective elongation was 3.6% and 3.3%, indicating a slight drop after the addition of the SiC nanoparticles due to the increased porosities introduced in the stir mixing process.

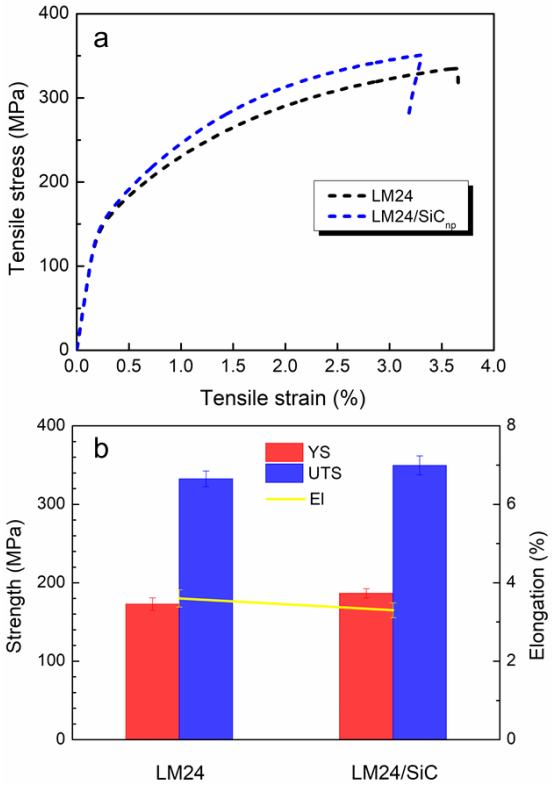

Figure 8 (a) Tensile stress-strain curves for the LM24 alloy and LM24/SiC$_{np}$ composite with the tensile properties shown in (b).

3.5 Fractography

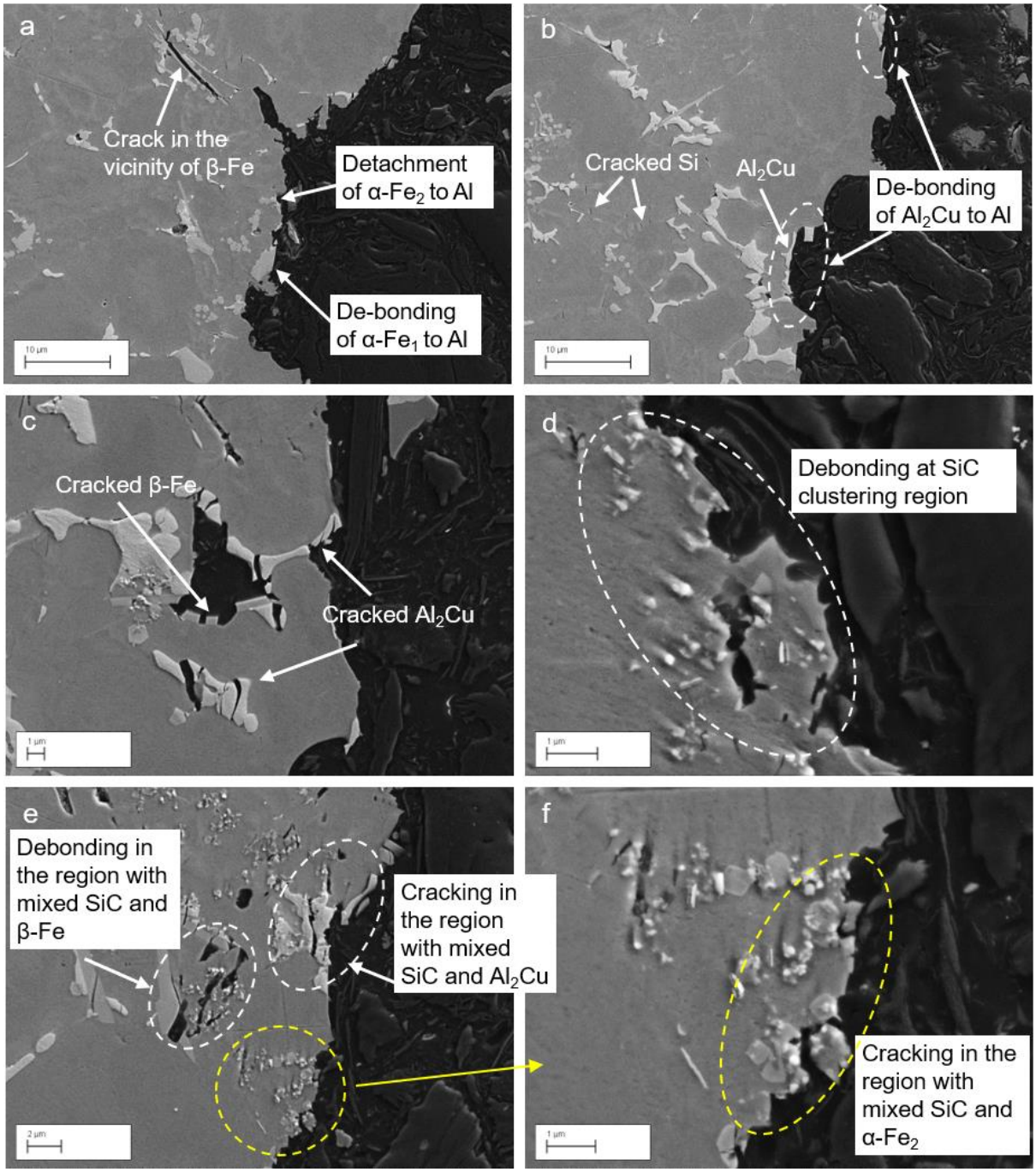

Figure 9 The SEM micrographs showing the crack structure on the longitudinal cross-section of (a, b) LM24 alloy and (c, d, e, and f) the LM24/SiC_{np} composites subjected to the tensile test.

Figure 9 shows the fracture microstructure on the longitudinal cross-section of the LM24 alloy and LM24/SiC_{np} composite subjected to tensile tests. The debonding/detachment of the α-Fe intermetallic phase (both $\alpha\text{-}Fe_1$ and $\alpha\text{-}Fe_2$) to the adjacent Al can be observed, as indicated in Figure 9a. Also, an evident crack along the β-Fe/Al interface was present, which was located in the region containing a cluster of Fe-bearing intermetallic phase. Similar debonding behaviour between the Al_2Cu intermetallic phase and Al matrix can be seen in Figure 9b, as indicated by the white-dash ellipses. In addition, cracked brittle Si particles were exhibited. The interfaces between

the intermetallic phase and Al matrix are prone to debonding under external stress, making them the vulnerable sites for crack initiation and subsequent propagation under further stress. The small cracks propagate and connect, leading to the final fracture of the material. In the case of LM24/SiC_{np} composite, in addition to the cracked Fe-bearing and Cu-bearing intermetallic compounds (Figure 9c), the region where SiC nanoparticles were agglomerated was the additional site for the crack initiation, due to the ease of debonding between SiC nanoparticles and Al matrix, as shown in Figure 9d. Moreover, the areas containing mixed SiC agglomerations and Fe-bearing and/or Cu-bearing intermetallic phase could add to the vulnerable sites for crack initiation and propagation, as readily indicated in Figure 9e and 9f. This could be detrimental to the ductility of the composites.

4 Discussions

4.1 Distribution of SiC nanoparticles and grain refinement

It has been confirmed that the relatively good distribution of the loose SiC agglomerates was achieved, despite that these loose agglomerates were mainly located in the interdendritic regions or the eutectic regions. This, to a large extent, suggested that a good dispersion of the particles in the molten metal was obtained under the combined effects of the physical pre-mixing and ultrasonic processing. On the other hand, a homogeneous dispersion of the individual SiC nanoparticles was not perfectly achieved, indicating that majority of the SiC nanoparticles were pushed rather than engulfed by the solidification front (solid-liquid interface) during the solidification process. When the molten metal containing suspended SiC nanoparticles solidified, interactions between the solidification front and the SiC nanoparticles occurred, resulting in the redistribution of the SiC particles. The SiC nanoparticles were either engulfed by the solidification front, and thus distributed in the interior of the grain, or pushed by the solid-liquid interface toward the grain boundaries or eutectic regions. For a given particle size, it was suggested [40,41] that a critical velocity of the solidification front can be calculated to push the particles by the solid-liquid interface, which is the solidification velocity above which particles are engulfed by the interface and below which they are pushed.

Whether the particle expulsion or engulfment occur is an extremely complicated phenomenon. To put it simply, the repulsive force from interfacial energy change and the dragging force resulting from the flow of liquid are considered the two main parameters [42,43] determining the critical velocity for a certain particle in a given melt. The repulsive force and the dragging force compete with each other. If the repulsive force outstrips the dragging force, particles will be pushed, inversely, the particles will be engulfed. The critical velocity of the solidification front will be calculated supposing the two opposite forces are equal. It has been largely reported that the critical velocity was increased with the decrease of particle sizes [42,44,45,46]. A higher cooling rate is more likely to cause a more homogeneous nanoparticle distribution. However, in our cases, even though a very high cooling rate can be achieved by the high pressure die casting process, the formation of the majority engulfment for the nanosized reinforcing particles was not successfully achieved, at least not in current experimental conditions.

The pushing nanoparticles or particle agglomerates could restrict the grain growth, depending on (1) how the lower thermal conductivity of the particle affects the temperature gradient ahead of the solidification front and therefore acts as a barrier to the removal of the heat necessary for further solidification; and (2) how the solid particle acts as a barrier preventing solute diffusion away from the tip of the growing dendrite, thereby changing

the concentration gradient and restricting growth. In our case, there is a nearly 40% decrease in the α-Al grains, from ~23.7 um to ~14.8 um, indicating a good grain growth restriction effect.

4.2 Strengthening mechanisms

The mechanical results have proved that the hardness and yield strength were improved by ~8%, after 1wt% addition of SiC nanoparticles (Figure 7 and 8). The improvement of strength can be ascribed to the combined effects of reduced Al grain size, CTE mismatch between SiC particles and Al matrix, Orowan strengthening etc. It was evidenced by the EBSD observations from Figure 4 that the α-Al grain size was decreased from ~23.7 μm to ~14.8 μm, which increased the yield strength according to the Hall-Petch relation [47], the difference in the yield strength after addition of the particles can be termed as:

$$\Delta\sigma_y = k\left(\frac{1}{\sqrt{d_{comp}}} - \frac{1}{\sqrt{d_{base}}}\right)$$

Where $\Delta\sigma_y$ is the change of the yield strength by the reduced grains; d_{comp} and d_{base} represents the grain size of the LM24/SiC$_{np}$ composite and the LM24 alloy, respectively. k is the strengthening coefficient. in the case of Al-Si alloys, the value of k can be set as 60 MPa μm$^{-1/2}$ [48]. If we take d_{comp} and d_{base} to be 23.7 μm and 14.8 μm, the $\Delta\sigma_y$ will be about 3MPa, which is minimal as the grain size for the HPDC alloy is already fine enough and the reduction of the grain size from 23.7 μm to 14.8 μm provide a limited contribution to the improvement of yield strength. Thus, the strengthening effect of this mechanism can be considered minor.

As the Al alloy matrix and SiC particles have different coefficients of thermal expansion (CTE), during cooling of the composite melt in the solidification process, a great number of dislocations will be generated due to thermal mismatch between the matrix and the SiC particles to accommodate the inconsistency of geometry variations. This will cause a high work hardening rate and a great strengthening effect. On the other hand, the nanoparticles or the clusters as a whole were the fine-sized hard obstacles that can strengthen the materials by pinning the movement of the dislocations, i.e. Orowan strengthening [48]. The elongation was decreased slightly after the 1wt% addition of SiC nanoparticles, which was due to the increased porosities and the extra crack-vulnerable sites containing the mixed agglomerates of SiC particles and the intermetallic phase, as shown in the fracture micrographs in Figure 9.

5 Conclusions

The present work prepared the LM24/SiC$_{np}$ composite by combining the advantages of stir mixing, ultrasonic treatment, and high pressure die casting which generating a high cooling rate, in an attempt to explore the effect of nanosized SiC particulates on the microstructure and mechanical properties of LM24 alloy. The following conclusions can be drawn:

- A relatively uniform distribution of the loose SiC agglomerates was obtained in the LM24/SiC$_{np}$ composite, which was resulted from the fine grain structure obtained in the HPDC process subjected to high cooling rates. On the other hand, the majority of the SiC nanoparticles were distributed in the interdendritic regions because these nanoparticles tended to be pushed rather than engulfed by the solidification front even though the melt solidified at a high cooling rate.

- The hardness and the yield strength were improved by ~7.7% and ~8% after the addition of 1wt% SiC nanoparticles due to a combined strengthening effect from grain refinement, Orowan strengthening mechanism and different coefficient of thermal expansion (CTE), with a slight drop in the elongation from 3.6% to 3.3%, ascribed to the added porosities and the crack-vulnerable sites containing the mixed nanoparticles and the Fe-bearing and Cu-bearing intermetallic phase.

Acknowledgement

Financial support from European Union (LIGHTME Grant Agreement No. 814552) is gratefully acknowledged. The authors are also grateful to the Experimental Technical Centre (ETC) which provided access to the equipment for microstructural characterization.

References

1 Ramnath BV, Elanchezhian C, Annamalai RM, Aravind S, Atreya TS, Vignesh V, Subramanian C (2014) Aluminium metal matrix composites–a review. Rev. Adv. Mater. Sci. 38(5):55-60.
2 Chawla NC, Chawla KK (2006) Metal-matrix composites in ground transportation. JOM 58(11):67-70.
3 Miracle DB (2005) Metal matrix composites–from science to technological significance. Compos. Sci. Technol. 65(15-16):2526-40.
4 Alaneme KK, Sanusi KO (2015) Microstructural characteristics, mechanical and wear behaviour of aluminium matrix hybrid composites reinforced with alumina, rice husk ash and graphite. Eng. Sci. Technol. Int. J. 18(3):416-22.
5 Shin JH, Choi HJ, Bae DH (2014) The structure and properties of 2024 aluminum composites reinforced with TiO2 nanoparticles. Mater Sci Eng A 607:605-10.
6 Dixit A, Kumar K (2015) Optimization of mechanical properties of silica gel reinforced aluminium MMC by using Taguchi method. Mater. Today: Proc. 2(4-5):2359-66.
7 Alizadeh A, Abdollahi A, Biukani H (2015) Creep behavior and wear resistance of Al 5083 based hybrid composites reinforced with carbon nanotubes (CNTs) and boron carbide (B4C). J Alloys Compd 650:783-93.
8 Krasnowski M, Gierlotka S, Kulik T (2015) TiC–Al composites with nanocrystalline matrix produced by consolidation of milled powders. Adv Powder Technol 26(5):1269-72.
9 Rahman MH, Al Rashed HM (2014) Characterization of silicon carbide reinforced aluminum matrix composites. Procedia Eng 90:103-9.
10 Sharma P, Sharma S, Khanduja D (2015) Production and some properties of Si3N4 reinforced aluminium alloy composites. J. Asian Ceram. Soc. 3(3):352-9.
11 Jia L, Kondoh K, Imai H, Onishi M, Chen B, Li SF (2015) Nano-scale AlN powders and AlN/Al composites by full and partial direct nitridation of aluminum in solid-state. J Alloys Compd 629:184-7.
12 Smith CA (2001) Discontinuous reinforcements for metal-matrix composites. Materials Park, OH: ASM International 2001:51-5.
13 Mavhungu ST, Akinlabi ET, Onitiri MA, Varachia FM (2017) Aluminum matrix composites for industrial use: advances and trends. Procedia Manuf. 7:178-82.
14 Tjong SC, Mai YW (2008) Processing-structure-property aspects of particulate-and whisker-reinforced titanium matrix composites. Compos. Sci. Technol. 68(3-4):583-601.
15 Srivastava N, Chaudhari GP (2016) Strengthening in Al alloy nano composites fabricated by ultrasound assisted solidification technique. Mater Sci Eng A 651:241-7.
16 Habibnejad-Korayem M, Mahmudi R, Poole WJ (2009) Enhanced properties of Mg-based nano-composites reinforced with Al2O3 nano-particles. Mater Sci Eng A 519(1-2):198-203.
17 Nguyen QB, Gupta M (2008) Enhancing compressive response of AZ31B magnesium alloy using alumina nanoparticulates. Compos. Sci. Technol. 68(10-11):2185-92.
18 Dieter GE (1986) Mechanical Metallurgy, third edition, McGraw-Hill (NY), New York.
19 Dai LH, Ling Z, Bai YL (2001) Size-dependent inelastic behavior of particle-reinforced metal–matrix composites. Compos. Sci. Technol. 61(8):1057-63.
20 Vogt R, Zhang Z, Li Y, Bonds M, Browning ND, Lavernia EJ, Schoenung JM (2009) The absence of thermal expansion mismatch strengthening in nanostructured metal–matrix composites. Scr. Mater 61(11):1052-5.
21 Brown LM, Stobbs WM (1976) The work-hardening of copper-silica v. equilibrium plastic relaxation by secondary dislocations. Philos Mag 34(3):351-72.

22 Schultz BF, Ferguson JB, Rohatgi PK (2011) Microstructure and hardness of Al2O3 nanoparticle reinforced Al–Mg composites fabricated by reactive wetting and stir mixing. Mater Sci Eng A 530:87-97.
23 Ferguson JB, Sheykh-Jaberi F, Kim CS, Rohatgi PK, Cho K (2012) On the strength and strain to failure in particle-reinforced magnesium metal-matrix nanocomposites (Mg MMNCs). Mater Sci Eng A 558:193-204.
24 Attar S, Nagaral M, Reddappa HN, Auradi V (2015) A review on particulate reinforced aluminum metal matrix composites. J. Emerg. Technol. Innov. Res. 2(2):225-9.
25 Ardakani MR, Khorsand S, Amirkhanlou S, Nayyeri MJ (2014) Application of compocasting and cross accumulative roll bonding processes for manufacturing high-strength, highly uniform and ultra-fine structured Al/SiCp nanocomposite. Mater Sci Eng A 592:121-7.
26 Naher S, Brabazon D, Looney L (2007) Computational and experimental analysis of particulate distribution during Al–SiC MMC fabrication. Compos. Part A Appl. Sci. Manuf. 38(3):719-29.
27 Hashim J, Looney L, Hashmi MS (1999) Metal matrix composites: production by the stir casting method. J. Mater. Process. Technol. 92:1-7.
28 Segurado J, Gonzalez C, Llorca J (2003) A numerical investigation of the effect of particle clustering on the mechanical properties of composites. Acta Mater 51(8):2355-69.
29 Nair SV, Tien JK, Bates RC (1985) SiC-reinforced aluminium metal matrix composites. Int. Mater. Rev. 30(1):275-90.
30 Lloyd DJ (1991) Aspects of fracture in particulate reinforced metal matrix composites. Acta Metall. Mater. 39(1):59-71.
31 Cao G, Konishi H, Li X (2008) Mechanical properties and microstructure of SiC-reinforced Mg-(2, 4) Al-1Si nanocomposites fabricated by ultrasonic cavitation based solidification processing. Mater Sci Eng A 486(1-2):357-62.
32 Suslick KS, Didenko Y, Fang MM, Hyeon T, Kolbeck KJ, McNamara III WB, Mdleleni MM, Wong M (1999) Acoustic cavitation and its chemical consequences. Philosophical Transactions of the Royal Society of London. Series A: Mathematical, Physical and Engineering Sciences 357(1751):335-53.
33Eskin, DG (2017) Ultrasonic processing of molten and solidifying aluminium alloys: overview and outlook, Mater. Sci. Technol. 33:6, 636-645.
34 Eskin GI (1998) Ultrasonic treatment of light alloy melts. Amsterdam, Gordon and Breach OPA.
35 Ji S, Yan F, Fan Z (2015) Development of a high strength Al–Mg2Si–Mg–Zn based alloy for high pressure die casting. Mater Sci Eng A 626:165-74.
36 Dandekar CR, Shin YC (2012) Modeling of machining of composite materials: a review. Int. J. Mach. Tools Manuf. 57:102-21.
37 Li Q, Rottmair CA, Singer RF (2010) CNT reinforced light metal composites produced by melt stirring and by high pressure die casting. Compos Sci Technol 70(16):2242-7.
38 Hu Q, Zhao H, Li F (2017) Microstructures and properties of SiC particles reinforced aluminum-matrix composites fabricated by vacuum-assisted high pressure die casting. Mater Sci Eng A 680:270-7.
39 Zhang Y, Wang S, Lordan E, Wang Y, Fan Z (2019) Improve mechanical properties of high pressure die cast Al9Si3Cu alloy via dislocation enhanced precipitation. J Alloys Compd 785:1015-22.
40 Sen S, Dhindaw BK, Stefanescu DM, Catalina A, Curreri PA (1997) Melt convection effects on the critical velocity of particle engulfment. J Cryst Growth 173(3-4):574-84.
41 Youssef YM, Dashwood RJ, Lee PD (2005) Effect of clustering on particle pushing and solidification behaviour in TiB2 reinforced aluminium PMMCs. Compos. Part A Appl. Sci. Manuf. 36(6):747-63.
42 Uhlmann DR, Chalmers B, Jackson KA (1964) Interaction between particles and a solid-liquid interface. J Appl Phys 35(10):2986-93.
43 Chen XH, Yan H (2016) Solid–liquid interface dynamics during solidification of Al 7075–Al2O3np based metal matrix composites. Mater Des 94:148-58.
44 Schultz BF, Ferguson JB, Rohatgi PK (2011) Microstructure and hardness of Al2O3 nanoparticle reinforced Al–Mg composites fabricated by reactive wetting and stir mixing. Mater Sci Eng A 530:87-97.
45 Stefanescu DM, Dhindaw BK, Kacar SA, Moitra A (1998) Behavior of ceramic particles at the solid-liquid metal interface in metal matrix composites. Metall Trans A 19(11):2847-55.
46 Stefanescu DM, Juretzko FR, Catalina A, Dhindaw BK, Sen S, Curreri PA (1998) Particle engulfment and pushing by solidifying interfaces: Part II. Microgravity experiments and theoretical analysis. Metall Mater Trans A 29(6):1697-706.
47 Hansen N (2004) Hall–Petch relation and boundary strengthening. Scr. Mater 51(8):801-6.
48 Gutierrez-Urrutia I, Munoz-Morris MA, Morris DG (2007) Contribution of microstructural parameters to strengthening in an ultrafine-grained Al–7% Si alloy processed by severe deformation. Acta Mater 55(4):1319-30.